Production of Rubidium Bose-Einstein Condensates at a 1 Hz Rate

Daniel M. Farkas,[1] Evan A. Salim,[1] and Jaime Ramirez-Serrano[1]

[1] *ColdQuanta, Inc., 1600 Range St., Suite 103, Boulder, CO 80301**

(Dated: March 20, 2014)

We present an experimental apparatus that produces Bose-Einstein condensates (BECs) of ^{87}Rb atoms at a rate of 1 Hz. As a demonstration of the system's ability to operate continuously, 30 BECs were produced and imaged in 32.1 s. Without imaging, a single BEC could be produced in 953 ms. The system uses an atom chip to confine atoms in a dimple trap with frequencies exceeding 1 kHz. With this tight trap, the duration of evaporative cooling was reduced to less than 0.5 s. Using principal component analysis, insight into the largest sources of noise and drift was obtained by extracting the dominant contributions to the variance. The system utilizes a compact physics package that can be integrated with lasers and electronics to create a transportable ultracold-atom device for applications outside of a laboratory environment.

While devices based on cold and ultracold neutral atoms offer unprecedented accuracy and precision for a wide variety of applications, the long times needed to cool atoms into the degenerate regime limit the bandwidths that can be achieved from sensors and devices that utilize ultracold matter. A typical laboratory-based apparatus can produce a Bose-Einstein condensate (BEC) in tens of seconds, corresponding to a sensor with a measurement bandwidth less than 0.1 Hz [1, 2]. Compare this, for example, to MEMS-based or laser-based inertial sensors, which typically operate at bandwidths of at least 1 kHz, high enough to accurately measure rapidly varying signals that are of interest for navigation. For ultracold atoms to compete with existing technologies, the production rates of BECs, quantum gases, and coherent atom sources must improve. Specific applications that would benefit from faster ultracold-atom production include timekeeping [3–5], inertial sensing [6–12], gravimetry [13, 14], electromagnetic field sensing [15, 16], atomtronics [17–19] and space-based experiments and devices [20, 21].

As a step towards rapid generation of ultracold matter, we present an apparatus that produces ^{87}Rb BECs at a rate of 1 Hz. The system's capabilities are demonstrated in Fig. 1, which shows pictures of 30 BECs produced and imaged in 32.1 s. Without imaging, a single BEC could be produced in 953 ms, corresponding to a production rate that exceeds 1 Hz. The apparatus and techniques described in this work show the extent to which speed improvements can be attained when ultracold matter is generated in a pulsed fashion. Given the engineering challenges associated with developing continuous coherent atomic sources (e.g. an "atom laser"), ultracold-atom devices operating in a pulsed mode remain a viable path toward developing high-bandwidth ultracold-atom sensors [22–28].

As shown in Fig. 2, the apparatus described here is one of the first to have demonstrated BEC production from a hot vapor in less than 1 s [29–33]. At 0.75 s, the fastest experiment produces ^{84}Sr BECs using direct laser cooling to degeneracy, a technique that works well for strontium due to the presence of a narrow-linewidth cooling transition that permits Doppler cooling to temperatures below 1 μK [29]. All the other experiments represented in the plot use ^{87}Rb. With the exception of the data point at 3.3 s, which corresponds to an optical trap [33], all of the rubidium-based experiments use atoms that are magnetically confined with an atom chip.

Forced evaporative cooling, which is one of the slowest steps of BEC production, is made more efficient by implementing it in a very tight magnetic dimple trap created with an atom chip [34–36]. The atom chip forms the top wall of a two-chamber ultrahigh vacuum system whose compact size allows for quick loading of a 3D MOT and fast transport of atoms to the atom chip [32, 37].

In addition to speed, ultracold-atom devices must be able to produce samples of ultracold atoms whose proprieties (e.g. number, condensate fraction, position) are stable over time. To that end, we applied principal component analysis to the BEC images in Fig. 1 [38]. The characteristic spectrum of eigenvalues obtained from this analysis serves as a baseline for repeatability, and can help identity and eliminate sources of noise and drift in the system. For the data set shown in Fig. 1, most of the variance can be attributed to the first three principal components. From plots of these dominant eigenvectors, we can identify fluctuations in atom number and the vertical position of the cloud.

In the first part of this paper, we present an overview of the BEC apparatus, including the vacuum system, atom chip, coils and magnets, physics package, and laser system. We then describe our experimental procedure, including the operating values used to create BECs in less than 1 s, followed by our implementation of absorption imaging. To characterize the performance of our vacuum system, we present typical data from two diagnostic tests: the 3D MOT lifetime and the magnetic chip-trap lifetime. Finally, we present the results of principal component analysis.

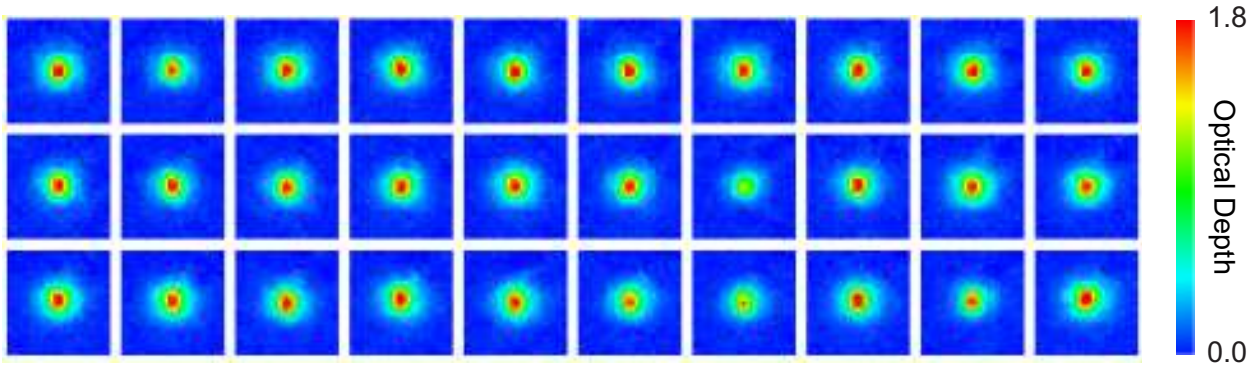

FIG. 1. Absorption images of 30 ^{87}Rb BECs produced and imaged in 32.1 s. Without imaging, a single BEC could be produced in 953 ms, corresponding to a production rate that exceeds 1 Hz.

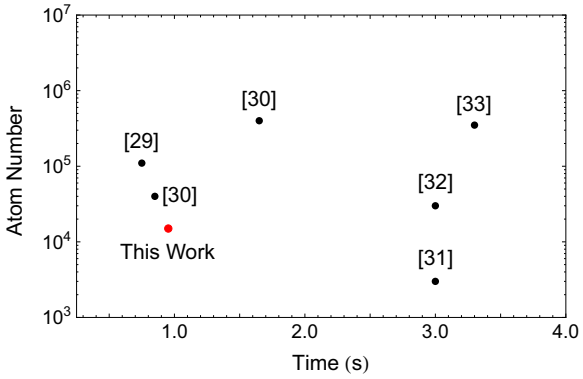

FIG. 2. Production speeds and atom numbers for some of the fastest reported BEC experiments [29–33]. The experiment described in this work is one of three to have reported a BEC production time of less than 1 s. For Ref. [30], two data points are plotted: one optimized for speed and one optimized for atom number.

APPARATUS

Vacuum Chamber and Atom Chip

The ultrahigh vacuum system (ColdQuanta RuBECi) utilizes a two-chamber configuration in which a 2D+ magneto-optical trap (MOT) in one chamber feeds a 3D MOT in a second chamber (see Fig. 3) [32, 37]. Differential pumping between the chambers is introduced by a 0.75 mm diameter pinhole in a silicon disc. With this differential pumping, rubidium pressures of 10^{-7} Torr can be created in the lower chamber while pressures below 10^{-9} Torr can be maintained in the upper chamber. A 2 l/s ion pump helps maintain vacuum.

The background rubidium vapor in the lower chamber is produced by running a current between 3.5 and 3.8 A through an alkali metal dispenser. A few milliwatts of laser light produces a vertically-oriented "push" beam that forces atoms through the pinhole and into the upper chamber, where they are collected in a 3D MOT. Reflection of the push beam off the silicon disc in the region around the pinhole produces additionally cooling in the third dimension, thereby forming a 2D+ MOT [39].

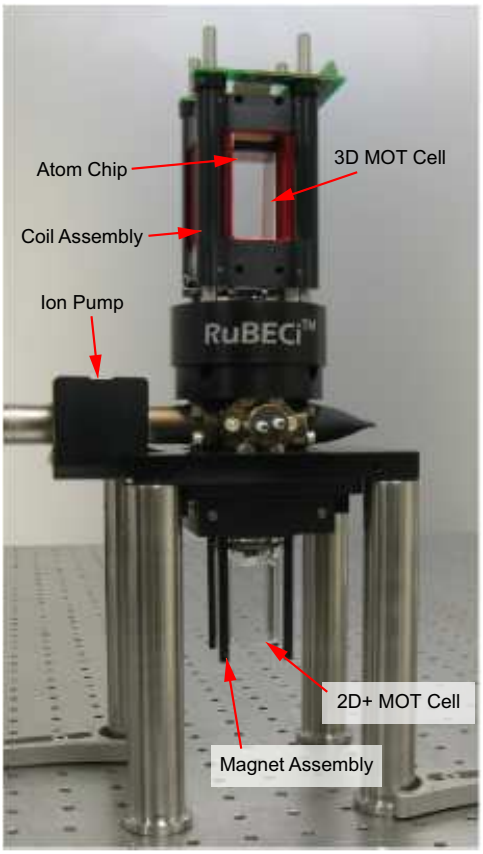

FIG. 3. The vacuum system consists of two chambers separated by a pinhole. In the lower chamber, a 2D+ MOT creates a cold-atom beam that feeds a 3D MOT in the upper chamber. An atom chip is bonded to the top of the upper chamber, where it forms a wall of the vacuum system. Vacuum is maintained with a 2 l/s ion pump.

Bonded to the top of the upper chamber of the vacuum system is the atom chip shown in Fig. 4. The atom chip

has dimensions of 23 × 23 mm and a thickness of 420 μm. The substrate contains regions of both glass and silicon, and through-chip vacuum-compatible electrical vias. The vacuum side of the chip contains copper traces that can be configured to produce a variety of chip-based Z-traps and dimple traps. The traces used in this work have widths of 100 μm and thicknesses of 10 μm.

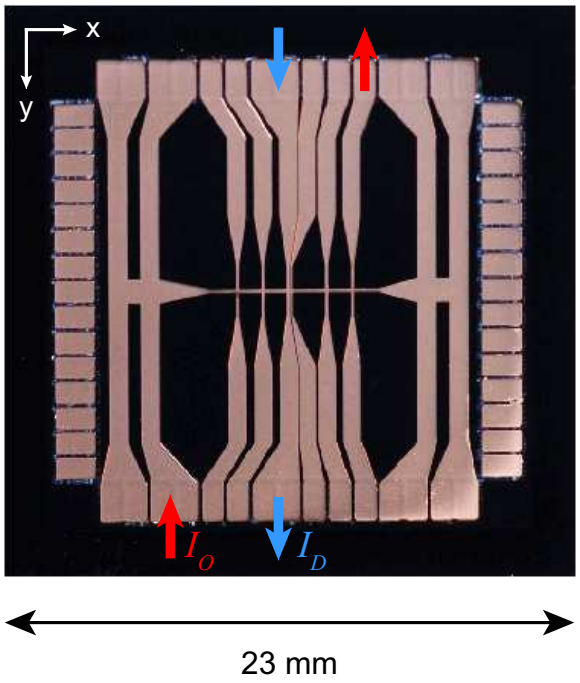

FIG. 4. The vacuum side of the atom chip consists of copper traces that can be configured to produce a variety of chip-based Z-traps and dimple traps. The red and blue arrows indicate the traces and currents used to create the dimple trap for this work. In this photograph, the left side of the atom chip is closest to the ion pump (see Fig. 3).

The duration of evaporative cooling was reduced to less than 0.5 s by utilizing a dimple trap with high trap frequencies [31, 40]. This trap was formed by running currents $I_0 = +3.25$ A and $I_D = +1.3$ A through two traces that cross each other perpendicularly at the center of the chip. The directions of these currents are represented by the red and blue arrows, respectively, in Fig. 4. To complete the trap, external bias fields of +19.2 G and -39.8 G were applied along the x and y directions, respectively.

The trap parameters were calculated with the Biot-Savart law under the assumption that the chip traces consist of infinitely-thin current sheets having widths of 100 μm and various lengths. Fig. 5 shows the magnitude of the magnetic field along the three cardinal directions. The trap minimum of 3.1 G is located 154 μm beneath the chip surface. The trap frequencies are $2\pi\times$(1.96, 1.93, 0.35) kHz.

Physics Package

Shown in Fig. 6, the physics package consists of four stages that can be independently positioned along four stainless steel support rods. These stages serve as mounting baseplates for the vacuum system, free-space optics, magnets, coils, and cameras. The lowest layer, or base stage, serves as a foundation for the entire package, and contains optics for the 2D+ MOT push beam and a CCD camera for imaging the 2D MOT along the vertical axis.

Above the base stage is the 2D MOT stage. A fiber optic cable delivers MOT laser light (i.e. cooling and repumping light) to this stage, after which free-space optics provide beam shaping, polarization control, and beam splitting. These optics provide the correct beam configuration to produce a 2D+ MOT in the lower chamber of the vacuum system.

The second stage from the top is the cell stage. The center of the vacuum system is bolted to this stage, as well as the permanent magnet assembly used to create the 2D+ MOT. This stage also contains a fiber optic port, turning mirrors, and waveplates for directing an optical pumping laser beam through the upper chamber of the vacuum system.

On the top level, or 3D MOT stage, laser light delivered by a fiber optic cable is directed with free-space optics to provide the correct beam geometry for producing a 3D MOT in the upper chamber of the vacuum system. This stage also contains a fiber optic port and turning mirrors that direct an absorption laser beam through the cell and into a CCD camera (Basler Scout 1390fm with Infinity Photo-Optical InfiniMini lens system). The absorption laser beam propagates along the +y direction (using the coordinate system defined in Fig. 4). To quantify the size and loading rate of the 3D MOT, a biconvex lens images fluorescence photons onto a large-area silicon photodetector (Thorlabs PDA100A) [1].

Magnetic Field Coils

The magnetic quadrupole field for the 2D+ MOT is generated by a magnet assembly that surrounds the lower chamber of the vacuum system (see Fig. 7a). To maximize the cold-atom flux driven out of the 2D+ MOT with the vertical push laser beam, the magnets are mounted on a translation stage that is used to align the MOT axis with the pinhole. The magnetic field gradient is approximately 37 G/cm.

All of the magnetic bias and quadrupole fields in the needed for the upper chamber are produced by the coil assembly shown in Fig. 7b. This assembly consists of six rectangular coils arranged as a square cuboid. The four rectangular coils on the sides each have a nominal DC resistance of 2.4 Ω, and an inductance of 0.92 mH (at 1 kHz). When the two coils aligned along the x-axis are

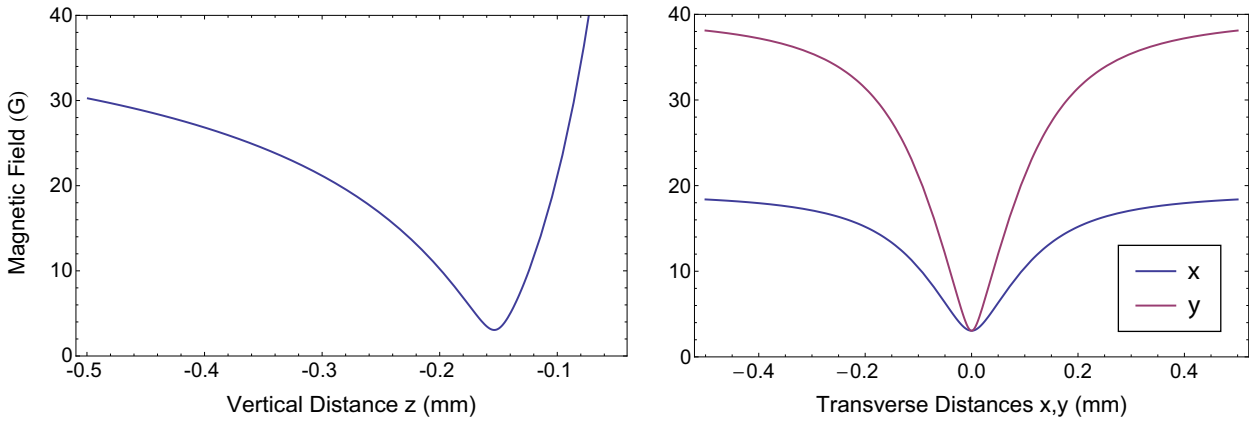

FIG. 5. To increase the speed of evaporative cooling, a chip-based dimple trap with high trap frequencies was used. These plots show the calculated magnitude of the trap's magnetic field along the vertical direction (left) and transverse directions (right). By modeling the chip traces as infinitely-thin current sheets with finite width and length, the trap frequencies are $2\pi\times$ (1.96, 1.93, 0.35) kHz. The trap minimum of 3.1 G is located at z =154 μm beneath the chip surface. Negative values of z indicate that the trap is centered beneath the atom chip.

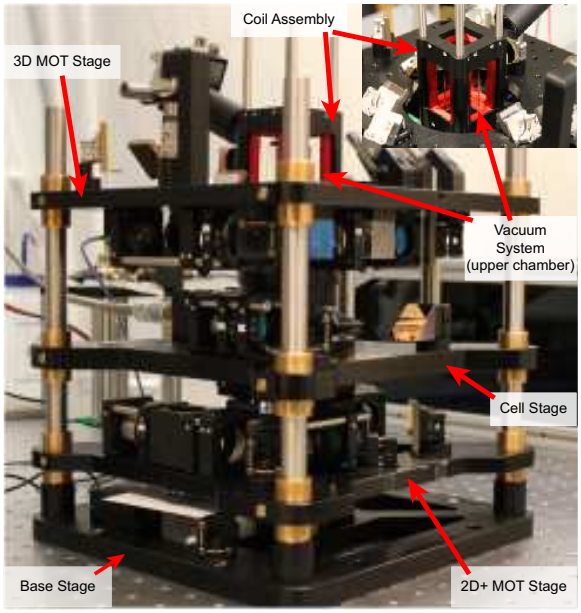

FIG. 6. Consisting of four stages, the physics package serves as a mounting structure for the vacuum system, free-space optics, magnets, coils, and cameras. The transfer Z-coil and CCD camera are not shown.

driven with currents of the same magnitude and opposite sign, they produce at the center of the assembly a gradient of (15.1, 11.0, 4.0) G/cm/A. When these currents have the same sign, the coils produce a bias field of +22.6 G/A $\hat{x}$. The y-axis coils are connected in series to produce a bias field of +22.6 G/A $\hat{y}$. The square coils at the top and bottom are connected in series to produce a bias field of +15.6 G/A $\hat{z}$. Each of these coils has a nominal DC resistance of 3.7 Ω and an inductance of 1.75 mH (at 1 kHz). Measurements of these gradients and bias fields agree with the calculated values listed here to within a few percent.

Cold atoms are transported vertically from the center of the 3D MOT cell to the atom chip using a transfer "Z" coil (see Fig. 7c). In conjunction with external bias fields, this coil creates a Ioffe-Pritchard whose height varies with current. This coil has a nominal DC resistance of 0.7 Ω and an inductance of 110 μH (at 1 kHz). Affixed to the bottom of the coil is an rf loop for evaporative cooling. The coil is mounted above the vacuum system such that the rf loop is situated less than 1 mm above the ambient side of the atom chip.

Laser System

Consisting entirely of commercially available components, the laser system uses three distributed bragg reflector (DBR) diode lasers (Vescent Photonics D2-100-DBR-780) operating near the rubidium D_2 line at 780.24 nm (see Fig. 8). As shown in Fig. 8, the stability of a frequency-stabilized master laser is transferred to the other lasers via optical phase-locked loops (PLLs).

The frequency of the master laser is locked to the $F = 2 \rightarrow F' = 3, 4$ crossover resonance in ^{85}Rb using a Doppler-free saturated absorption spectrometer (Vescent Photonics D2-110-Rb) and servo electronics (Vescent Photonics D2-125-PL-T). To generate a zero-crossing error signal suitable for frequency stabilization, 4 MHz frequency sidebands are imposed on the master laser via modulation of the laser current. The cooling laser is phase-locked approximately 1.5 GHz to the red of the master laser, placing it near the ^{87}Rb $F = 2 \rightarrow F' = 3$ cooling transition. Similarly, the repumping laser frequency is phase-locked 4 GHz to the blue of the master

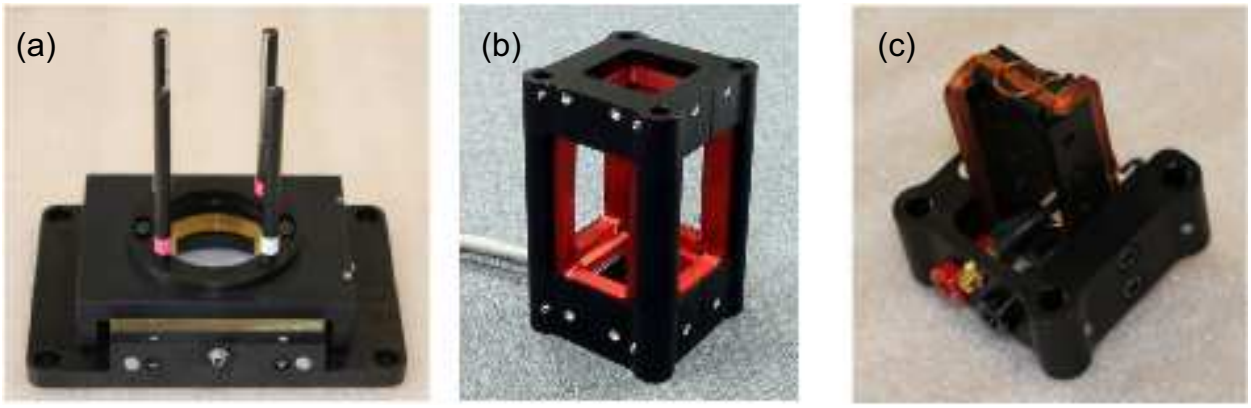

FIG. 7. (a) The quadrupole field for the 2D+ MOT is generated by a magnet assembly that surrounds the lower chamber of the vacuum system. The magnets are mounted on a stage for translating the position of the MOT axis. (b) Consisting of six coils arranged in a square cuboid, the coil assembly produces magnetic bias fields and gradients in the upper chamber of the vacuum system. (c) Laser-cooled atoms are transported vertically to the atom chip using a transfer "Z" coil whose windings have the same "Z" orientation as the chip trap. The circular windings in the center of the coil is an rf loop used for forced evaporative cooling.

laser, placing it at the ^{87}Rb $F = 1 \rightarrow F' = 2$ repumping transition.

Microwave beat notes between the lasers are generated using heterodyne modules (Vescent Photonics D2-150) that couple a few percent of the light from each beam into multimode fiber-optic patchcords. Each fiber delivers light to a high-speed photodetector that outputs a signal proportional to the difference frequency of the lasers. This difference frequency is divided by a prescaler; the phase of this lower frequency signal is then compared to a local oscillator using a digital phase/frequency detector (Vescent Photonics D2-135-FC-800) whose output is fed-back to the laser current controller (Vescent Photonics D2-105). The local oscillator is a rf voltage-controlled oscillator tuned with an external analog voltage.

After passing through their respective heterodyne modules, the outputs of the cooling and repumping lasers are overlapped using a half-waveplate and polarized beamsplitter cube (PBS). A second half-waveplate and PBS set the ratio of cooling and repumping powers, and project the two components onto the same polarization axis. This dual-frequency beam is then coupled into a polarization-maintaining (PM) patchcord that delivers this light to the input of a tapered amplifier (TA; New Focus TA-7613-P). About 15 mW of laser light is used to seed the tapered amplifier. Although the TA can output up to 500 mW, it is operated at lower drive currents so that it outputs only 200 mW.

In addition to a 40 dB optical isolator housed inside each laser module, an additional 40 dB isolator (Optics For Research IO-3D-780-VLP) was placed after each laser to block reflections originating from the output faces of the multimode patchcords. Reflections from the fiber input of the TA are minimized with the use of FC/APC connectors. However, when the TA is turned on, back-reflected light into the input fiber causes multimode operation. To block this light, an additional 40 dB optical isolator was placed in front of the PM fiber coupler.

As shown in Fig. 9, the TA output is split into three beams: one for the 2D MOT, one for the 3D MOT, and one for both optical pumping and imaging. To ensure the high extinction ratios needed for BEC production, each beam path contains a mechanical shutter (Stanford Research Systems SR-475 or SR-476). The transition time of each shutter was decreased to approximately 100 μs by placing it at the center of a 1:1 telescope formed from a pair of f=30 cm plano-convex lenses. The three beams are then coupled into PM fiber patchcords that deliver the light to the experiment. For the pumping/imaging beam, transition times less than 1 μs are achieved with a pair of fiber-optic shutters connected in series (Agiltron SWDR-112211112 and NSSW-127115333). The 2D MOT and 3D MOT fiber patchcords deliver 75 mW and 50 mW, respectively, of combined cooling and repumping power to the experiment, while the fiber shutter outputs provide 0.5 mW of total power for optical pumping and imaging.

To minimize reflections, all of the PM patchcords that deliver light to the physics package use FC/APC connectors. To ensure the long-term stability of the polarization at the fiber outputs, a half-waveplate and quarter-waveplate are used to precisely align the laser polarization with the fiber axis.

BEC PRODUCTION

In this section, we summarize the experimental procedure for producing BECs. As shown in Table I, the sequence is divided into a series of stages, each with their

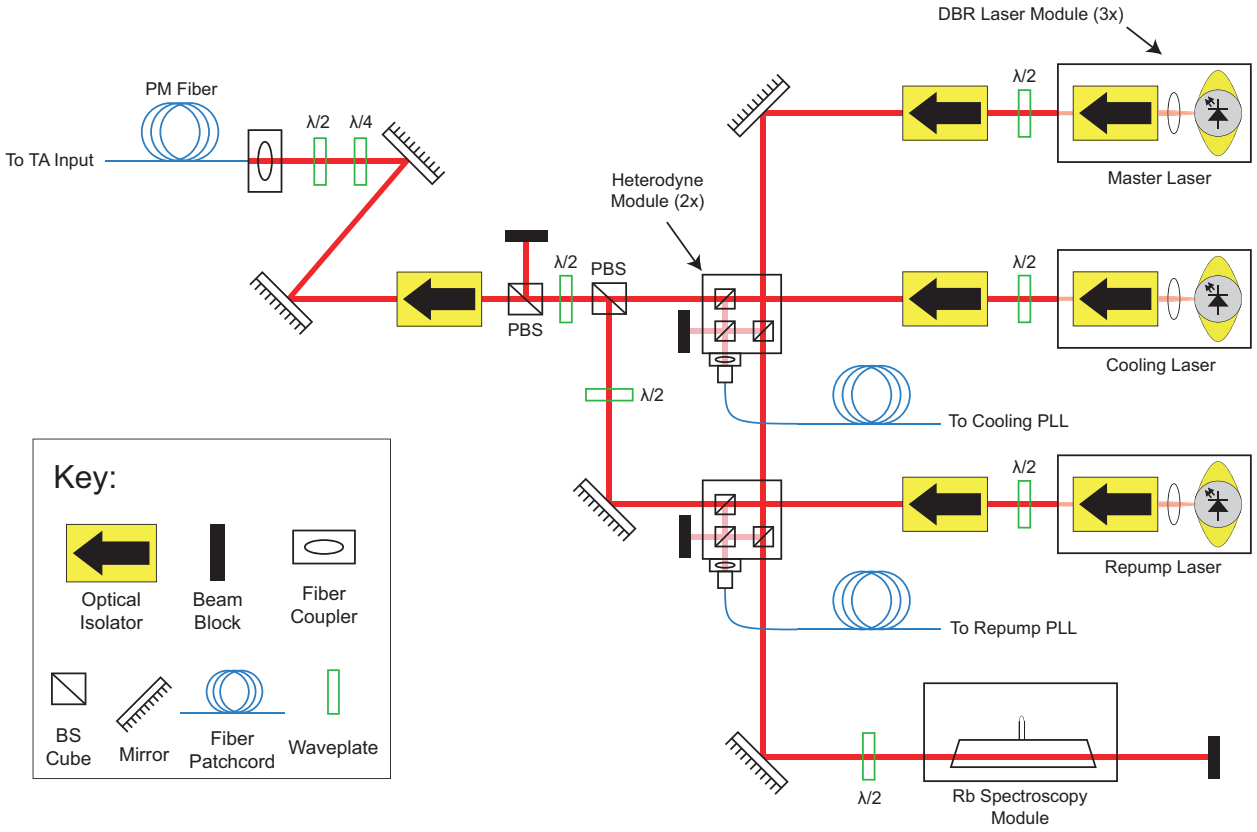

FIG. 8. The laser system consists of three distributed bragg reflector (DBR) diode lasers at 780.24 nm. A master laser is locked to a rubidium vapor cell and serves as a stable optical frequency reference; its stability is transferred to the other lasers via optical phase-lock loops. Light at the cooling and repumping transitions is combined into a single beam and amplified up to 200 mW with a tapered amplifier.

own values for laser parameters, magnetic fields, chip currents, and RF driving fields.

The BEC production sequence starts by loading approximately 5×10^8 ^{87}Rb atoms into a 3D MOT that is centered in the upper chamber of the vacuum system. These atoms are loaded from the 2D+ MOT produced in the lower vacuum chamber. The 2D+ MOT is generated with 72 mW of combined cooling and repumping laser power, of which a few milliwatts is split off to form the vertically oriented push beam [39]. The 3D MOT is generated with 50 mW of combined laser power. The two MOTs are created with light from the same lasers, and therefore both have the same cooling laser detuning of -2.5 Γ, where $\Gamma = 6.0$ MHz is the natural linewidth of the rubidium D_2 transition.

To make this stage as short as possible, the cold-atom flux produced by the 2D+ MOT is maximized by running the rubidium dispenser at 3.8 A. At this current, the 3D MOT loading rate is 4×10^9 atoms/s. Operating the dispenser at higher currents did not increase the 3D MOT loading rate.

After loading, the 3D MOT is spatially compressed by decreasing the cooling laser detuning to -4.5 Γ and increasing the magnetic field gradient by a factor of 4.8 [41]. Atoms are allowed to accumulate in the dark $F = 1$ ground hyperfine state by blue-detuning the repumping laser frequency by 140 MHz.

With spatial compression, the cloud of atoms can be moved upward while still being fully illuminated by all of the laser beams. Moving the atoms upward places them closer to the atom chip, which reduces the amount of current needed to initially trap the atoms with the Z-coil. The atoms are moved upward, typically by 1 to 2 mm, by changing the vertical bias field.

The atoms are cooled below the Doppler limit with a few milliseconds of polarization gradient cooling [42]. Here, the cooling laser is red-detuned by 110 MHz, or -10.3 Γ, while the repumping laser is on-resonance. Small magnetic bias fields cancel stray fields, particularly those from the nearby ion pump magnets. The cloud's temperature is typically lowered to between 25 and 50 μK, as determined from resonant absorption imaging of the cloud size for various expansion times.

To maximize the number of atoms that are magnetically trapped and transported to the atom chip, the atoms are optically pumped into the magnetically trap-

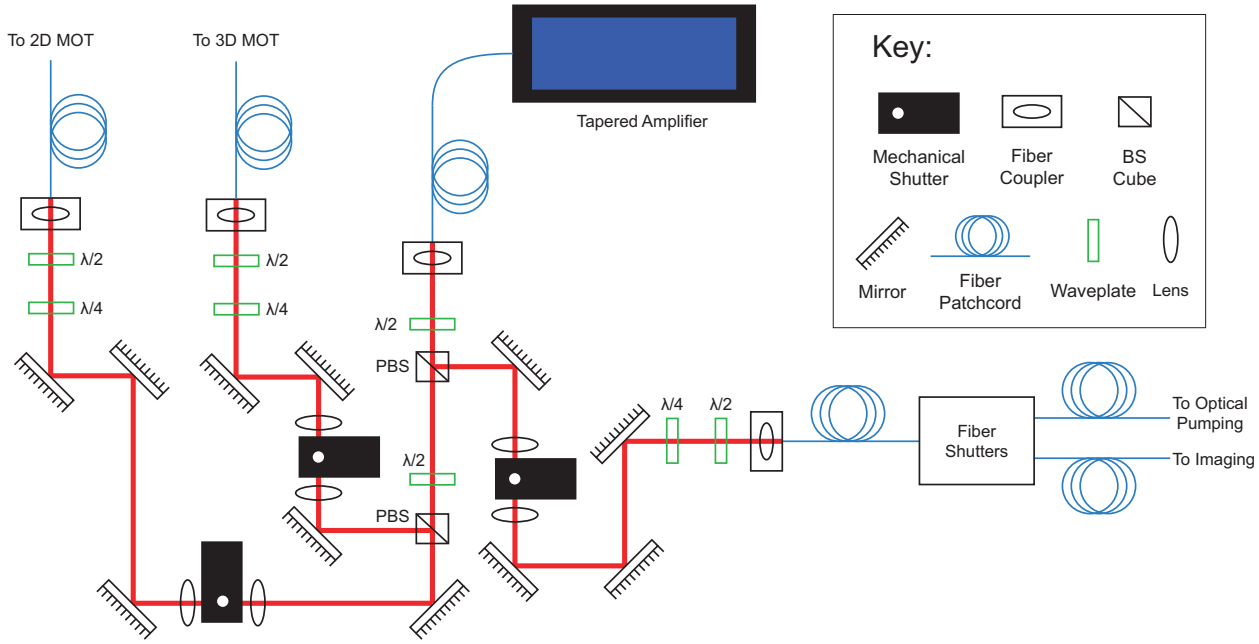

FIG. 9. The 200 mW output of the tapered amplifier is split into three beams. All patchcords shown use PM fiber and FC/APC connectors. The 2D MOT and 3D MOT fiber patchcords deliver 75 mW and 50 mW, respectively, of combined cooling and repumping power to the experiment. For optical pumping and imaging, a pair of fiber-optic shutters deliver 0.5 mW to the experiment.

pable $|F = 2, m_F = +2\rangle$ state. Compared to atom capture without optical pumping, this stage typically increases the number of chip-trapped atoms by a factor of 2.5. Here, a magnetic bias field is applied along the x direction. Approximately 0.5 mW of optical pumping light passes through a quarter-waveplate to become circularly polarized, and propagates through the cell along the -x direction. The cooling laser is red-detuned by 235 MHz, placing its frequency approximately $5.2\,\Gamma$ to the blue of the $F = 2 \rightarrow F' = 2$ transition.

The remaining stages of BEC production require no laser light, and all of the laser beams are now mechanically shuttered to prevent stray photons from heating the atoms and inhibiting condensation. The optically pumped atoms, which are positioned slightly above the center of the cell, are transported vertically to the atom chip using a magnetic trap created by the external Z-coil and bias coils. With almost 20 A of current flowing through the Z-coil, the position of the initial trap coincides with the cloud. Linearly reducing this current moves the trap position upward. To prevent excess heating of the atoms during transport, the ramp is made adiabatic by extending its duration to more than 200 ms.

Atoms are transferred from the Z-coil trap into the chip trap by ramping the Z-coil current to 0 A. At the beginning of this ramp, the atom chip currents are turned on to their final values of 3.25 A and 1.3 A for the main trace and dimple trace, respectively. We also investigated a transfer scheme in which the chip currents were linearly increased to their final values as the Z-coil current was linearly reduced to 0 A; with this technique, we observed fewer atoms in the final chip trap.

Evaporative cooling is implemented with a series of linear frequency ramps from 35 to approximately 1 MHz [43]. As shown in Table I, the five ramps last only 475 ms. The RF drive power is set to 0.07, 0.28, 0.57, 0.57, and 0.11 W (rms into a 50 Ω load) for stages A through E, respectively.

After the cloud has condensed, the chip trap is adiabatically decompressed by reducing the x and y bias fields to 1/3 of their nominal values. Decompressing the trap reduces the condensate's chemical potential. This smaller potential also lowers the energy gradient, which in turn reduces the rate at which the condensate expands when it is dropped. By slowing down this expansion, it is easier to visually identify condensed atoms from thermal atoms (which expand at a rate determined solely by their temperature).

IMAGING

Pictures of BEC clouds are taken using standard absorption imaging with a laser pulse resonant with the $F = 2 \rightarrow F' = 3$ transition. To improve the quality of the data, two images are taken. The first, or "signal", image is taken after the atoms have fallen under the influence of gravity for a time-of-flight (TOF) typically between 2 and 10 ms. The second, or "background", image

Stage	Time (ms)	Δ_c (MHz)	Δ_r (MHz)	B_{x1} (A)	B_{x2} (A)	B_y (A)	B_z (A)	Z-Coil (A)	I_0 (A)	I_D (A)	RF Freq. (MHz)
3D MOT Loading	125	-15	0	0.58	-0.5	-0.085	0.36				
Compression	25	→ -27	→ 140	→ 3	→ -2.2	→ -0.17	→ 0.1				
PGC	3.32	-110	0	-0.002		-0.014	0.046				
Optical Pumping	0.85	-235	0	-0.1		0	0				
Z-Coil Loading	3			-0.3		-0.5	0.5	19.5			
Z-Coil Transport	210			→ 0.25		→ -1.80	→ 0	→ 7			
Chip Transfer	85			→ 0.85		→ -1.76	0	→ 0	3.25	1.3	
Evaporation A	110			0.85		-1.76	0		3.25	1.3	35 → 20
Evaporation B	120			0.85		-1.76	0		3.25	1.3	→ 14
Evaporation C	130			0.85		-1.76	0		3.25	1.3	→ 5
Evaporation D	90			0.85		-1.76	0		3.25	1.3	→ 2
Evaporation E	25			0.85		-1.76	0		3.25	1.3	→ 1.14
Decompression	20			→ 0.283		→ -0.587	0		3.25	1.3	
Imaging - Atoms	5.28	0	0	0		0	0				
Imaging - Back.	60	-15	0	0		0	0				

TABLE I. Experimental parameters for producing BECs at a rate of 1 Hz. An arrow indicates a linear ramp; the arrow points to the ending value while a blank space to the left of an arrow indicates that the initial value of the ramp is equal to the value of that parameter at the end of the previous stage. The detuning of the cooling and repumping lasers from their respective resonances are denoted by Δ_c and Δ_r; blank spaces in these two columns indicate that all laser beams have been shuttered. All magnetic fields are expressed in terms of drive currents and can be converted into magnetic field units using the numerical factors listed in the text. The coil labeled "x1" is located on the side of the vacuum system closest to the ion pump. Currents through the main and dimple traces of the atom chip are denoted by I_0 and I_D, respectively. Blank spaces in the Z-coil and chip current columns indicate no current, while blank spaces in the RF frequency column indicate that the frequency generator is disabled. The duration of the first imaging stage includes a 5 ms time-of-flight expansion.

is taken without the atoms; it essentially records optical artifacts, the most prevalent of which are diffraction rings caused by dust, optical imperfections, and clipping of the laser beam. The optical depth OD_i of pixel i is defined as $\mathrm{OD}_i = 10\log_{10}(b_i/s_i)$ where s_i is the value of the pixel in the signal image and b_i is the value of the same pixel in the background image. A complete OD plot is obtained by repeating this calculation for each of the 1392×1040 pixels comprising the images.

The duration τ_P of the laser pulses is typically $40\,\mu$s, a value that represents a trade-off between competing necessities: on the one hand, the image duration should be as short as possible in order to capture the atoms' instantaneous positions and to prevent smearing due to their motion. At the same time, the duration should be long enough to ensure that the pixels register values close to, but not reaching, their maximum value of $2^{12} = 4096$; this ensures the camera's full dynamic range is utilized. Taken together, these two constraints would lead one to conclude that short, intense laser pulses are ideal. However, the laser intensity should not saturate the atomic transition, as the calculation of OD does not account for such nonlinear effects. Here, a laser power of 1 mW and beam diameter of 1 cm correspond to an intensity of $0.6\,\mathrm{mW/cm^2}$; the corresponding saturation parameter is $S = 0.18$. With this constraint on laser intensity, the camera pixels approach, but do not exceed, saturation for $\tau_P = 40\,\mu$s. The camera is programmed to provide no additional internal gain.

Ideally, optical artifacts will appear identically in both signal and background images, and therefore will cancel in the OD plot. However, mechanical vibrations can cause these artifacts to shift by several pixels in the interim between the two images. This results in imperfect cancellation that usually manifests itself as visible striations (i.e ridges and valleys) in the OD plots. To minimize this effect, the delay between the images should be made as short as possible, and preferably less than the period of a typical acoustic vibration (e.g. $\ll 1$ ms).

For commercially available scientific CCD cameras, the minimum time delay between back-to-back exposures is usually limited by the speed with which the image is transferred from the camera to a computer. The CCD camera used here utilizes a FireWire 800 link, which can upload a full image of 1392×1040 12-bit pixels in 60 ms.

To circumvent this long transfer time, the camera is operated in "overlapped exposure mode" in which the background exposure occurs at the same time as the signal image is uploaded. The background exposure cannot finish until the signal image has been completely transmitted. As a result, the background exposure must last at least 60 ms. However, the background exposure can begin as soon as $\tau_D = 0.2$ ms after the signal exposure ends.

The timing diagram of Fig. 10 shows how overlapped exposure mode reduces the delay time between images.

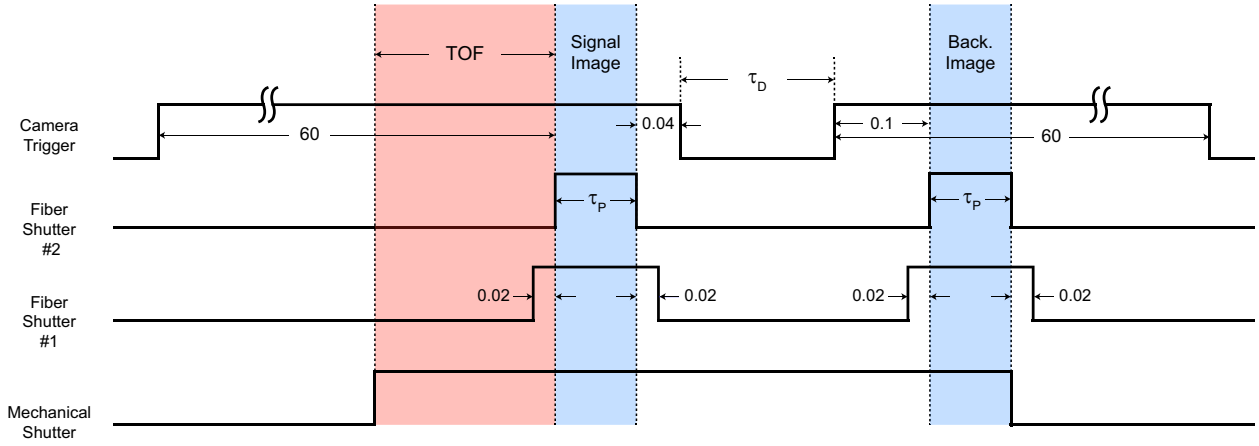

FIG. 10. Timing diagram for implementing overlapped exposure mode of the CCD camera. By taking the signal image at the end of the first 60 ms exposure, and the background image at the beginning of the second 60 ms exposure, the delay time between images can be reduced to less than 0.5 ms. Here, $\tau_D = 0.2$ ms is the minimum delay time between exposures and $\tau_P = 40\,\mu$s is the duration of the absorption laser pulses. Acquisition of the signal and background images is represented by the blue shading. The time-of-flight (TOF) is represented by the red shading. All durations listed are in milliseconds. The first imaging stage in Table I starts with the time-of-flight.

Here, the signal image is acquired at the end of the first exposure. The background image is then taken at the beginning of the second exposure. The time delay between images is reduced by more than a factor of 100 to less than 0.5 ms. The images coincide with the opening of the second fiber shutter. To reduce stray light while the mechanical shutter is open, the first fiber shutter is opened 20 μs before the second fiber shutter opens, and is closed 20 μs after the second fiber shutter closes.

With overlapped exposure, the delay between images is so short that the atoms can appear in both the signal and background images. To prevent this, the laser frequency is detuned by -15 MHz in the interim between images. An alternative approach is to drive current through one of the coils, using the generated magnetic field to induce a Zeeman shift that moves the atomic resonance by approximately 1.4 MHz/G. The challenge with this approach is overcoming the coil's inductance, which works to oppose the flow of current, in such a short time. As a result, the Z-coil is preferable for this approach, as it has it has several times less inductance than the coils that comprise the coil assembly.

Overlapped exposure mode only constrains the duration of the second exposure. To ensure that the camera dark current contributes equal background levels to the two images, both exposure durations are set to 60 ms. In this case, the first exposure will begin (60 ms - TOF) before the start of the imaging stage. When the first exposure begins during evaporation, Z-coil transport, or chip transfer, all of the lasers are shuttered, blocking stray laser photons from reaching the camera. However, when imaging atoms immediately after a stage when the lasers are not shuttered (e.g. compression or PGC), the camera will be exposed to scattered light. To prevent this, the first exposure should be shortened so that it begins immediately after the lasers are shuttered.

DIAGNOSTICS AND CALIBRATION

We present two tests for evaluating vacuum performance: 3D MOT lifetime measurements and magnetic trap lifetime measurements. In addition, to calibrate the atom number for absorption images, the image size per pixel is obtained by dropping cold clouds of atoms for various time-of-flights.

3D MOT Lifetime

Decay of the 3D MOT is a useful diagnostic tool for initially verifying that the vacuum quality in the upper chamber is adequate for BEC production. Fig. 11 shows a typical decay curve, as measured with the fluorescence photodetector in the physics package. At earlier times, decay is dominated by excited-state trap-loss collisions (i.e. fine-structure-changing collisions and radiative escape) that depend on the atom density, laser detuning, and laser intensity [44]. In the tail of the decay, the atom density is low enough that loss is dominated instead by one-body collisions with the background gas. By fitting the tail to the sum of an exponential decay and constant offset, the time constant due to the vacuum exceeds 100 s (see inset of Fig. 11).

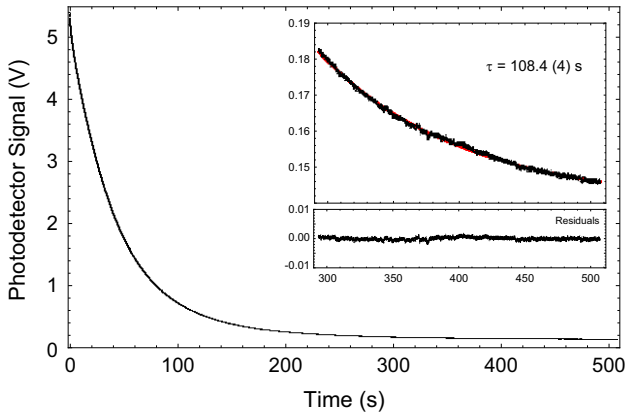

FIG. 11. The vacuum quality in the upper chamber of the vacuum system can be initially quantified by measuring the decay of the 3D MOT. In the tail of the decay curve, the effects of excited-state trap-loss collisions are negligible, leaving one-body collisions as the dominant loss mechanism. For this data set, the 3D MOT was created with 44 mW of combined cooling and repumping light, as measured at the output of the 3D MOT fiber coupler on the physics package. The data points in the tail were fit to the sum of an exponential decay and constant offset using a Levenberg-Marquardt algorithm; the best-fit curve is shown in red (see inset).

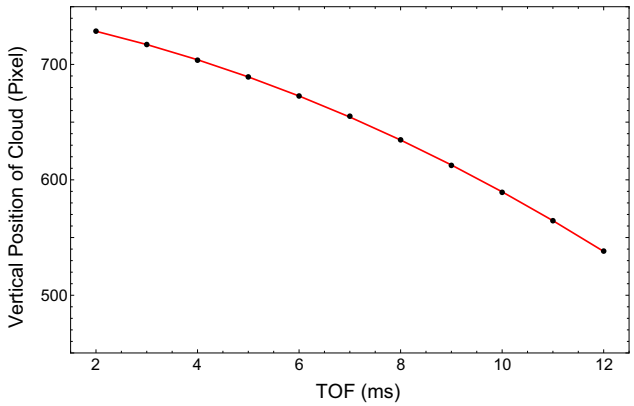

FIG. 12. After partial evaporation in the chip trap, thermal clouds are dropped for various time-of-flights (TOFs). The vertical positions of these dropped clouds form a parabola, from which the image size of a single CCD pixel is determined to be $k = 5.82(9)\,\mu$m/pixel.

Calibrating Atom Number

The number of atoms N can be obtained from an OD image with the formula

$$N = \frac{k^2}{\sigma_0} \sum_l \mathrm{OD}_l, \tag{1}$$

where the sum is taken over pixels in the region-of-interest, and $\sigma_0 = 0.1356\,\mu\mathrm{m}^2$ is the resonant cross-section of the $F = 2 \rightarrow F' = 3$ transition. The factor k gives the image size (in units of length) of a single camera pixel.

To measure k, clouds are released from the same initial chip trap for various time-of-flights between 2 and 12 ms. For each time-of-flight t_i, the OD image of the cloud is fit to a two-dimensional Gaussian, from which the center coordinates (in units of pixels) are extracted as best-fit parameters. When plotted versus time-of-flight, the vertical positions y_i form a parabola due to the influence of gravity (see Fig. 12).

Quantitatively, the points $y_i(t_i)$ are fit to the function $y_i = 1/2(g/k)t_i^2 + v_0 t_i + y_0$, where $g = 9.80\,\mathrm{m/s}^2$, v_0 is a small initial downward velocity imparted to the cloud when it is released at $t = 0$, and $y = 0$ is the initial vertical position. To narrow the clouds' profiles and increase OD, the atoms are partially evaporated in the atom chip before dropping. The data fit returns the value $k = 5.82(9)\,\mu$m/pixel. Here, we have assumed that one of the camera's axes aligns perfectly along the direction of gravity. Furthermore, the atom number calculated from Eqn. 1 is an underestimate due to the presence of a small amount of repumping light in the imaging laser beam.

Atom Chip Trap Lifetime

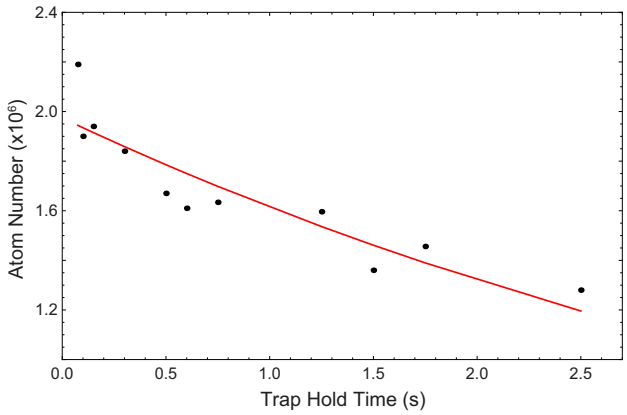

FIG. 13. Measured atom number as a function of hold time in a dimple trap. Fitting the atom numbers to an exponential function yields a $1/e$ trap lifetime of 5.0(8) s.

In addition to 3D MOT lifetime measurements, magnetic lifetime measurements are also useful for quantifying the residual background pressure in the upper chamber. As an example, Fig. 13 shows measured atom number as a function of hold time in a chip-based dimple trap. Here, atoms in the trap were first evaporatively cooled for 250 ms, after which the trap was decompressed by reducing the bias fields. The cloud was imaged after a 2 ms time-of-flight. The atom number was determined from the OD image using Eqn. 1. The atom numbers were fit to an exponential function, from which a $1/e$ lifetime of 5.0(8) s was obtained. Note that this lifetime is longer

than the duration of the evaporative cooling sequence (see Table I), as required for runaway evaporation.

DATA ANALYSIS

To characterize the repeatability and stability of BEC production, principal component analysis (PCA) was applied to the images in Fig. 1 [38]. Since each image was taken at a different time, all of the variance in the data set is attributed to time-varying processes. PCA can help identify the types and sources of noise and drift, and help distinguish fundamental noise processes (e.g. atom shot noise) from instrument-based systematics (e.g. temperature coefficients of electronic components). The main result of this analysis is an eigenvalue spectrum that quantifies the magnitude and distribution of variance in the data set. The eigenvalue spectrum can be used as a baseline to which other apparatus can be compared, or as an experimental "signal" to be minimized as part of an optimization sequence.

To perform PCA, the pixel values of each image were flattened to a one-dimensional array of length $m = 31 \times 31 = 961$. These arrays were used to construct a $m \times n$ matrix, where $n = 30$ is the number of samples for each pixel. For each of the m pixels, the mean value of that pixel was subtracted from each of its samples. The image corresponding to the mean values of the pixels is shown in the inset of Fig. 14.

The eigenvalues and eigenvectors of the covariance of this matrix were numerically calculated in Mathematica. The sorted eigenvalues are shown in red in Fig. 14. Most of the variance of the data set can be attributed to the first three eigenvalues. For comparison, if all of the variance in the data set arose from independent, identically distributed (i.i.d.) noise taken from a probability distribution with a well-defined mean and variance (e.g. white Gaussian noise), then the eigenvalue spectrum would be represented by the blue lines in Fig. 14. The distinct deviation from i.i.d. noise exhibited by the first few eigenvalues is a clear indication of noise and drift that is non-uniform, both temporally and spatially.

To help identify physical processes that are contributing to the large variances of the first few eigenvalues, Fig. 15 shows false-color plots of the first three eigenvectors. In Fig. 15a, the first eigenvector displays rotational symmetry about the location of the cloud's center. This eigenvector, which accounts for almost 40% of the variance of the data set, is most likely due to to atom number variation.

In Fig. 15b, the second eigenvector displays odd symmetry in the vertical direction about the position of the cloud's center, indicating fluctuations in the vertical position of the cloud. There is no principal component showing similar fluctuations in the horizontal direction. Possible explanations for this variation include timing jitter; changes in the chip trap's location due to noise and drift in the chip currents or magnetic bias fields; an initial downward velocity imparted to the cloud from an induced slosh mode; and mechanical vibration of either the camera, imaging lens, or vacuum cell.

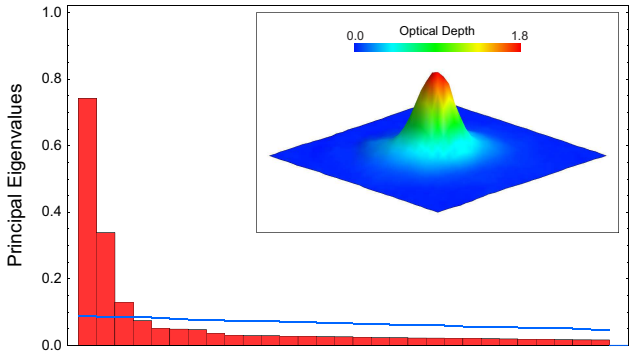

FIG. 14. Bar chart (red) of the ordered eigenvalues of the principal components of the data set in Fig. 1. The first three principal components account for most of the variance of the data set. The blue lines show how the distribution of eigenvalues for white Gaussian noise of equal variance. The image in the inset is comprised of the mean values of the pixels.

The third eigenvector, shown in Fig. 15c, contains a peak at the location of the cloud's center surrounded by a circular ring. We interpret this component to represent fluctuations in the condensate fraction. Indeed, the BECs used in the data set were only partially condensed in the hopes of exaggerating such an effect.

To relate the total variance of the data set to the mean image, a signal variance was calculated by summing the squares of the pixel values from the mean image. The result of 80.3, compared to the total variance of 1.94, implies that 2.4% of the energy in a single image is attributable to the effects identified by PCA. The largest principal component (PC), with a variance of 0.74, contributes 0.9% of the energy.

To obtain values for atom number, condensate fraction, and cloud position, and to characterize the repeatability and stability of these parameters, we chose to model each cloud as a two-dimensional bimodal distribution that represents the condensed core as a parabaloid and the thermal component as a Bose-enhanced Gaussian [45, 46]. Mathematically, this distribution $f(x, y)$ has the form

$$f(x,y) = A^{(th)}\ g_2\left\{\exp\left[-\left(\frac{x-x_0}{\sigma_x^{(th)}}\right)^2 - \left(\frac{y-y_0}{\sigma_y^{(th)}}\right)^2\right]\right\} + A^{(c)}\ \mathrm{Max}\left[1 - \left(\frac{x-x_0}{\sigma_x^{(c)}}\right)^2 - \left(\frac{y-y_0}{\sigma_y^{(c)}}\right)^2, 0\right] + C \quad (2)$$

where $g_j\{z\} = \sum_i z^i/i^j$, x_0 and y_0 are the center coordinates of the cloud, $\sigma_x^{(th)}$ and $\sigma_y^{(th)}$ are the widths of the thermal component along the x and y directions, $\sigma_x^{(c)}$ and

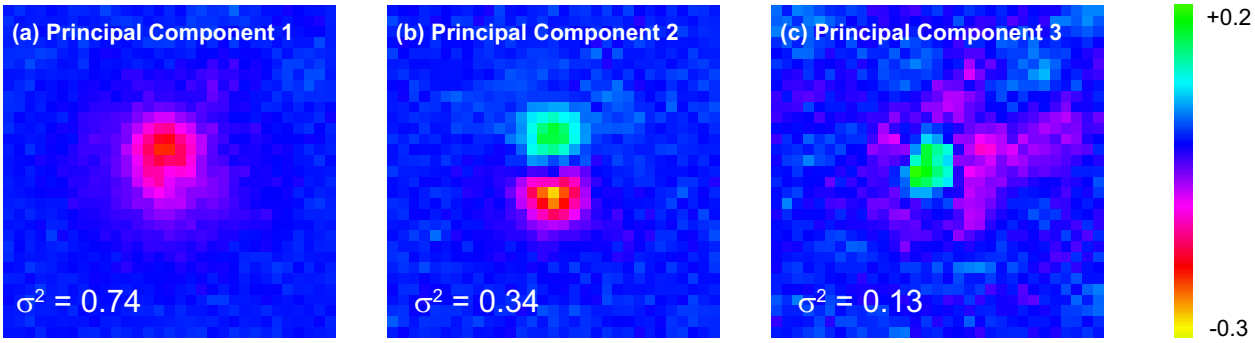

FIG. 15. The eigenvectors of the first three principal components show variance that is higher in the region of the cloud. In (a), the largest source of variance is most likely due to atom number variation. In (b), the variance is attributed to fluctuations in the vertical position of the cloud. The principal component in (c) is interpreted as fluctuations in the condensate fraction.

$\sigma_y^{(c)}$ are the widths of the condensed component along the x and y directions, and $A^{(th)}$ and $A^{(c)}$ are the amplitudes of the thermal and condensed components, respectively. C is a constant offset.

The condensate fraction $F = N_c/(N_c + N_{th})$ can be calculated from the numbers N_c and N_{th} of condensed and thermal atoms, respectively. Integrating the first two terms of Eqn. 2 over all space yields

$$N_c = \frac{2\pi}{5}\frac{A^{(c)}\sigma_x^{(c)}\sigma_y^{(c)}}{\sigma_0} \tag{3}$$

where $\sigma_0 = 0.1356\,\mu\text{m}^2$ is the resonant cross section for the $F = 2 \rightarrow F' = 3$ transition. Similarly,

$$N_{th} = g_3\{1\}\,\pi\frac{A^{(th)}\sigma_x^{(th)}\sigma_y^{(th)}}{\sigma_0} \tag{4}$$

where $g_3\{1\} = \zeta(3) \approx 1.202$. Here, the widths σ_x and σ_y are expressed in units of meters by multiplying their values in pixels by the calibration factor $k = 5.82\,\mu$m/pixel (see Fig. 12).

To filter the images in Fig. 1, each of the 30 images was reconstructed using the mean image and the first three PCs. Keeping these PCs ensures that the filtered images retain the key sources of variance. The other 27 PCs predominantly reflect i.i.d. noise that is more likely due to imaging than any true variation of the atom clouds. Therefore, discarding these PCs yields cleaner images while having negligible, if any, impact on our ability to characterize the BECs. As an example of filtering, Fig. 16 shows the first BEC image both before and after filtering. Here, the color scale has been magnified to highlight the noise reduction, especially in the blue region surrounding the cloud.

Each of the filtered BEC images was fit to Eqn. 2 using a Levenberg-Marquardt algorithm. Using the best-fit parameters, the cloud position (x_0, y_0), total atom number $N_c + N_{th}$, and condensate fraction F were calculated for each image. Figures 17a and b show the total atom number and condensate fraction, respectively, for each

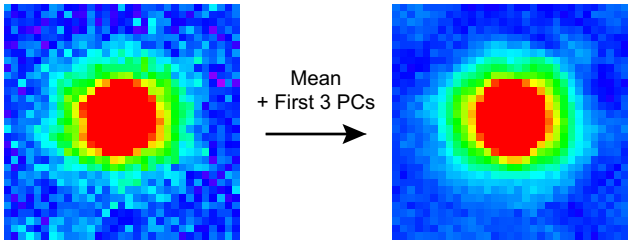

FIG. 16. Example of image filtering based on PCA. Here, the first BEC in Fig. 1 was reconstructed using the mean image (the inset of Fig. 14) and the first three principal components (see Fig. 15).

BEC in the sequence. For atom number, the mean is 26.2×10^3 atoms with a standard deviation of 3.2×10^3 atoms. For condensate fraction, the mean is 0.220 with a standard deviation is 0.023.

Fig. 17c shows the best-fit positions for the cloud centers. As expected, the standard deviation of 0.25 pixels in the vertical direction (blue points) is three times larger than the standard deviation of 0.07 pixels in the horizontal direction. Note that the variance in the vertical position appears to arise from an increase in shot-to-shot scatter, as opposed to a drift on longer timescales. This feature indicates that slow processes, such as temperature drift, are unlikely to explain the variance. Also note that the standard deviations of x_0 and y_0 are less than 1 pixel; this ability to determine positions at a level that exceeds the camera resolution is possible due to a signal-to-noise ratio greater than unity.

CONCLUSIONS

We presented an ultracold-atom system that is capable of producing ^{87}Rb BECs at a rate of 1 Hz. By confining the atoms in a tight dimple trap created with an atom chip, the duration of the evaporative cooling stage was reduced to less than 0.5 s. The system can operate

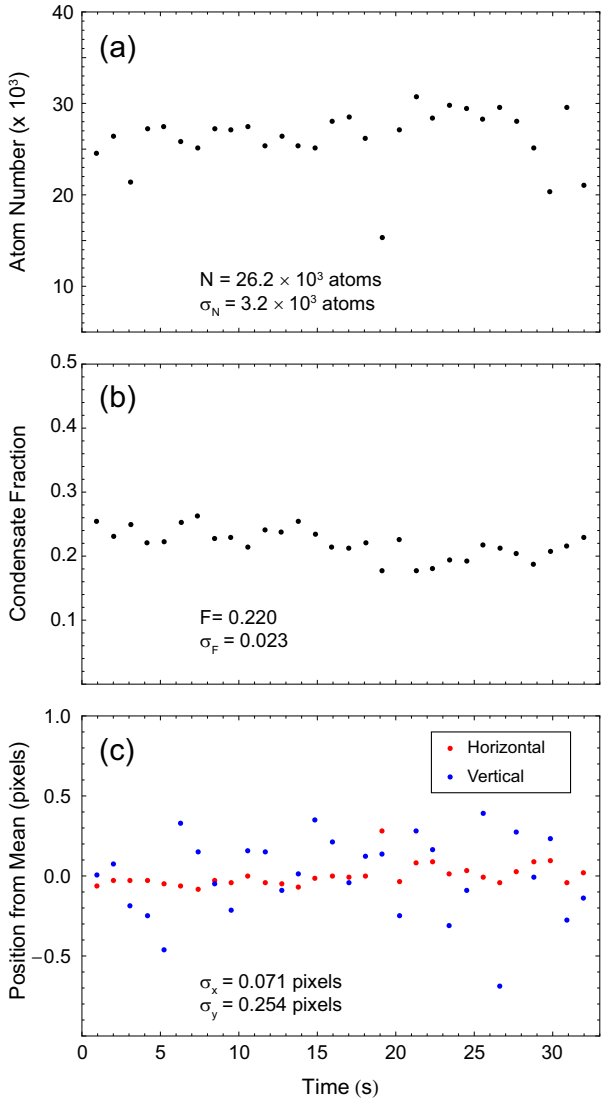

FIG. 17. Total atom numbers, condensate fractions, and cloud positions obtained from fitting each filtered BEC image to a bimodal distribution. The vertical position of the cloud has a standard deviation σ_y three times larger than that for the horizontal position (σ_x).

continuously, as demonstrated by the sequential creation and imaging of 30 BECs (see Fig. 1). Principal component analysis was used to study the variance of the BEC images and provide insight into some of the dominant sources of noise and drift. The system's speed, repeatability, and size make it a useful starting point for a portable ultracold-atom system designed for inertial sensing, gravimetry, and other applications outside of a laboratory environment.

This work was funded by the Office of Naval Research through their Small Business Innovation Research (SBIR) program (Contract Number N00014-10-C-0282).

* daniel.farkas@coldquanta.com

[1] H. J. Lewandowski, D. M. Harber, D. L. Whitaker, and E. A. Cornell, J. Low Temp. Phys. **132**, 309 (2003).
[2] E. W. Streed, A. P. Chikkatur, T. L. Gustavson, M. Boyd, Y. Torii, D. Schneble, G. K. Campbell, D. E. Pritchard, and W. Ketterle, Rev. Sci. Instrum. **77**, 023106 (2006).
[3] N. Hinkley, J. A. Sherman, N. B. Phillips, M. Schioppo, N. D. Lemke, K. Beloy, M. Pizzocaro, C. W. Oates, and A. D. Ludlow, Science Express (2013), 10.1126/science.1240420.
[4] B. J. Bloom, T. L. Nicholson, J. R. Williams, S. L. Campbell, M. Bishof, X. Zhang, W. Zhang, S. L. Bromley, and J. Ye, arXiv:1309.1137v2 (2013), 1309.1137.
[5] W. Maineult, C. Deutsch, K. Gibble, J. Reichel, and P. Rosenbusch, Phys. Rev. Lett. **109**, 020407 (2012).
[6] T. L. Gustavson, P. Bouyer, and M. A. Kasevich, Phys. Rev. Lett. **78**, 2046 (1997).
[7] T. L. Gustavson, A. Landragin, and M. A. Kasevich, Classical Quant. Grav. **17**, 2385 (2000).
[8] Y.-J. Wang, D. Z. Anderson, V. M. Bright, E. A. Cornell, Q. Diot, T. Kishimoto, M. Prentiss, R. A. Saravanan, S. R. Segal, and S. Wu, Phys. Rev. Lett. **94**, 090405 (2005).
[9] D. S. Durfee, Y. K. Shaham, and M. A. Kasevich, Phys. Rev. Lett. **97**, 240801 (2006).
[10] J. H. T. Burke and C. A. Sackett, Phys. Rev. A **80**, 061603(R) (2009).
[11] T. Berrada, S. van Frank, R. Bücker, T. Schumm, J.-F. Schaff, and J. Schmiedmayer, Nat. Commun. **4**, 2077 (2013).
[12] G. D. McDonald, H. Keal, P. A. Altin, J. E. Debs, S. Bennetts, C. C. N. Kuhn, K. S. Hardman, M. T. Johnsson, J. D. Close, and N. P. Robins, Phys. Rev. A **87**, 013632 (2013).
[13] A. Peters, K. Y. Chung, and S. Chu, Nature **400**, 849 (1999).
[14] J. M. McGuirk, G. T. Foster, J. B. Fixler, M. J. Snadden, and M. A. Kasevich, Phys. Rev. A **65**, 033608 (2002).
[15] S. Wildermuth, S. Hofferberth, I. Lesanovsky, S. Groth, P. Krüger, J. Schmiedmayer, and I. Bar-Joseph, Appl. Phys. Lett. **88**, 264103 (2006).
[16] P. Böhi, M. F. Riedel, T. W. Hänsch, and P. Treutlein, Appl. Phys. Lett. **97**, 051101 (2010).
[17] J. A. Stickney, D. Z. Anderson, and A. A. Zozulya, Phys. Rev. A **75**, 013608 (2007).
[18] R. A. Pepino, J. Cooper, D. Z. Anderson, and M. J. Holland, Phys. Rev. Lett. **103**, 140405 (2009).
[19] A. Ramanathan, K. C. Wright, S. R. Muniz, M. Zelan, W. T. Hill, C. J. Lobb, K. Helmerson, W. D. Phillips, and G. K. Campbell, Phys. Rev. Lett. **106**, 130401 (2011).
[20] F. Ramírez-Martínez, C. Lacroûte, P. Rosenbusch, F. Reinhard, C. Deutsch, T. Schneider, and J. Reichel, Adv. Space Res. **47**, 247 (2011).
[21] H. Müntinga *et al.*, Phys. Rev. Lett. **110**, 093602 (2013).
[22] M.-O. Mewes, M. R. Andrews, D. M. Kurn, D. S. Durfee, C. G. Townsend, and W. Ketterle, Phys. Rev. Lett. **78**, 582 (1997).
[23] I. Bloch, T. W. Hänsch, and T. Esslinger, Phys. Rev. Lett. **82**, 3008 (1999).

[24] A. P. Chikkatur, Y. Shin, A. E. Leanhardt, D. Kielpinski, E. Tsikata, T. L. Gustavson, D. E. Pritchard, and W. Ketterle, Science **296**, 2193 (2002).

[25] T. Lahaye, Z. Wang, G. Reinaudi, S. P. Rath, J. Dalibard, and D. Guéry-Odelin, Phys. Rev. A **72**, 033411 (2005).

[26] N. P. Robins, C. Figl, M. Jeppesen, G. R. Dennis, and J. D. Close, Nat. Phys. **4**, 731 (2008).

[27] G. L. Gattobigio, A. Couvert, G. Reinaudi, B. Georgeot, and D. Guéry-Odelin, Phys. Rev. Lett. **109**, 030403 (2012).

[28] E. P. Power, L. George, B. Vanderelzen, P. Herrera-Fierro, R. Murphy, S. M. Yalisove, and G. Raithel, arXiv:1202.0479 (2012).

[29] S. Stellmer, B. Pasquiou, R. Grimm, and F. Schreck, Phys. Rev. Lett. **110**, 263003 (2013).

[30] Waldemar Herr, private communication.

[31] M. Horikoshi and K. Nakagawa, Appl. Phys. B: Lasers Opt. **82**, 363 (2006).

[32] D. M. Farkas, K. M. Hudek, E. A. Salim, S. R. Segal, M. B. Squires, and D. Z. Anderson, Appl. Phys. Lett. **96**, 093102 (2010).

[33] T. Kinoshita, T. Wenger, and D. S. Weiss, Phys. Rev. A **71**, 011602(R) (2005).

[34] H. Ott, J. Fortagh, G. Schlotterbeck, A. Grossmann, and C. Zimmermann, Phys. Rev. Lett. **87**, 230401 (2001).

[35] W. Hänsel, P. Hommelhoff, T. W. Hänsch, and J. Reichel, Nature **413**, 498 (2001).

[36] J. Reichel, Appl. Phys. B: Lasers Opt. **74**, 469 (2002).

[37] E. A. Salim, J. DeNatale, D. M. Farkas, K. M. Hudek, S. E. McBride, J. Michalchuk, R. Mihailovich, and D. Z. Anderson, Quantum Inf. Process. **10**, 975 (2011).

[38] S. R. Segal, Q. Diot, E. A. Cornell, A. A. Zozulya, and D. Z. Anderson, Phys. Rev. A **81**, 053601 (2010).

[39] K. Dieckmann, R. J. C. Spreeuw, M. Weidemüller, and J. T. M. Walraven, Phys. Rev. A **58**, 3891 (1998).

[40] J. Reichel, W. Hänsel, P. Hommelhoff, and T. Hänsch, Appl. Phys. B: Lasers Opt. **72**, 81 (2001).

[41] W. Petrich, M. H. Anderson, J. R. Ensher, and E. A. Cornell, J. Opt. Soc. Am. B **11**, 1332 (1994).

[42] J. Dalibard and C. Cohen-Tannoudji, J. Opt. Soc. Am. B **6**, 2023 (1989).

[43] W. Ketterle and N. J. van Druten, in *Advances in Atomic, Molecular, and Optical Physics*, Vol. 37, edited by B. Bederson and H. Walther (Elsevier, 1996) pp. 181–236.

[44] J. Weiner, V. S. Bagnato, S. Zilio, and P. S. Julienne, Reviews of Modern Physics **71**, 1 (1999).

[45] Y. Castin and R. Dum, Phys. Rev. Lett. **77**, 5315 (1996).

[46] W. Ketterle, D. S. Durfee, and D. M. Stamper-Kurn, in *Bose-Einstein condensation in atomic gases, Proceedings of the International School of Physics "Enrico Fermi", Course CXL*, edited by M. Inguscio, S. Stringari, and C. E. Wieman (IOS Press, Amsterdam, 1999) pp. 67–176.